

Detection of Prostate Abnormality within the Peripheral Zone using Local Peak Information

Andrik Rampun¹, Paul Malcolm² and Reyer Zwiggelaar¹

¹Department of Computer Science, Aberystwyth University, Aberystwyth SY23 3DB, U.K.

²Department of Radiology, Norfolk & Norwich University Hospital, Norwich NR4 7UY, U.K.

Keywords: Computer Aided Detection of Prostate Cancer, Peak Detection, Prostate Abnormality Detection, Prostate MRI.

Abstract: In this paper, a fully automatic method is proposed for the detection of prostate cancer within the peripheral zone. The method starts by filtering noise in the original image followed by feature extraction and smoothing which is based on the Discrete Cosine Transform. Next, we identify the peripheral zone area using a quadratic equation and divide it into left and right regions. Subsequently, peak detection is performed on both regions. Finally, we calculate the percentage similarity and Ochiai coefficients to decide whether abnormality occurs. The initial evaluation of the proposed method is based on 90 prostate MRI images from 25 patients and 82.2% (sensitivity/specificity: 0.81/0.84) of the slices were classified correctly with 8.9% false negative and false positive results.

1 INTRODUCTION

In 2013, approximately 239,000 American men were diagnosed with prostate cancer (more than 20,000 increased compared to 217,730 cases in 2010 (Tempany and Franco, 2012)). In the United Kingdom, over 40,000 cases are reported annually with more than 10,000 deaths (PCUK, 2013). Generally, there are several well known clinical diagnostic tests such as prostate-specific-antigen (PSA) level (Brawer, 1991), digital rectal examination (DRE) (Shirley and Brewster, 2011), transrectal ultrasound (TRUS) (Aus et al., 2008) and biopsy tests (Roehl et al., 2002). Nevertheless, prostate cancer too often goes undetected as the sensitivity and specificity of these techniques could be improved and could have complications (Tidy, 2013; Kenny, 2012; Choi et al., 2007; Tempany and Franco, 2012). Prostate magnetic resonance imaging (MRI) can provide non-invasive imaging and in combination with computer technology can provide a detection tool which has the potential to improve the accuracy of clinical diagnostic tests (Ampeliotis et al., 2007). Figure 1 shows an example prostate MRI image with its ground truth delineated by an expert radiologist.

This research aims to develop a computer aided diagnosis (CAD) tool for prostate cancer by comparing data peaks between the left and right regions of the peripheral zone (PZ). Peak detection methods are

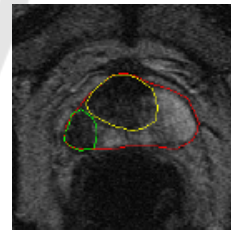


Figure 1: The ground truth of prostate gland, central zone and tumor are represented in red, yellow and green, respectively.

popular in many signal processing applications. However, not much work has been done applying such technique to the detection of prostate cancer based on MRI analysis. Limited number of methods in the literature attempted to use peak values in detecting prostate abnormality such as (Vos et al., 2010), (Reinsberg et al., 2007) and (Choi et al., 2007). A method proposed by (Vos et al., 2010) uses a peak detector to select abnormal regions from the obtained likelihood map constructed during the voxel classification stage. Subsequently, they perform automatic normalisation and histogram analysis for each of the abnormal regions before calculating malignancy using a supervised classifier. On the other hand, (Reinsberg et al., 2007) uses peaks information together with an apparent diffusion coefficient map to detect abnormality within the prostate. Another study by (Choi et al., 2007) shows that peak information has

the potential to improve the detection of prostate cancer in MR spectroscopy. In fact, it also allows detection of prostate cancer in the transitional zone. On the other hand, (Ampeliotis et al., 2007) used a combined feature vectors from MRI T-2 weighted images and Dynamic Contrast Enhanced (DCE) to increase the sensitivity of prostate cancer detection. (Engelbrecht et al., 2010) suggests new techniques such as dynamic contrast-enhanced MRI, diffusion-weighted imaging, and magnetic resonance spectroscopic imaging yield significant improvements in identification and volume estimation.

In this paper we propose a new method for detecting prostate abnormality within the peripheral zone based on peak information obtained from the extracted features. In contrast to the existing methods in the literature, our method is different in the sense that:

1. The proposed method does not use any supervised/unsupervised classifiers for likelihood classification of each region as used in (Vos et al., 2010) and (Ampeliotis et al., 2007).
2. We only used a single modality for abnormality detection which is T2-Weighted MRI. The method in (Engelbrecht et al., 2010) used multimodality such as diffusion MRI and MR Spectroscopy. Similarly, the method proposed in (Vos et al., 2010) used a multiparametric MR of T1- and T2-weighted imaging. (Choi et al., 2007) suggests that various techniques such as dynamic contrast materialenhanced MR imaging, diffusion-weighted imaging, and MR spectroscopy has the potential to improve the detection of prostate cancer. On the other hand (Reinsberg et al., 2007) combined the use of diffusion-weighted MRI and 1H MR Spectroscopy.
3. The proposed method is purely based on peak information obtained from extracted features. Unlike the method in (Vos et al., 2010) they used additional clinical diagnostic information such as biopsy tests in making decision as whether cancer is truly present or not.

2 PROSTATE MODELLING

Figure 2 shows a schematic overview of the prostate. Approximately 70% of prostate cancer can be found within the peripheral zone (PZ) and 30% within the central zone (CZ) and transitional zone (TZ) (Choi et al., 2007). Therefore, this method aims to detect prostate abnormality only within the PZ. We did not perform automatic prostate segmentation and the

prostates associated regions were delineated by an expert radiologist.

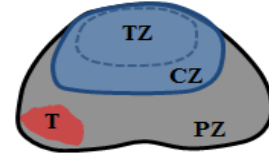


Figure 2: CZ = central zone, PZ = peripheral zone, TZ = transitional zone, T = tumor.

Based on the schematic overview shown in Figure 2, we defined our 2D prostate model in Figure 3. The prostate model has been recently proposed by (Rampun et al., 2013a). The prostate's PZ is defined using the quadratic equation $y = ax^2 + bx + c$ based on three crucial coordinate points of the prostate which are v_1, v_2 and v_3 . They are determined by the outmost x and y coordinates of the prostate boundary which are $x_{min}, x_{max}, y_{min}, y_{max}$ (see Figure 3). For example, x_{min} and y_{max} can be determined by taking the minimum and maximum x and y coordinates along the prostate boundary. Moreover, the x coordinates of v_1 and v_2 are captured from x_{min} and x_{max} and their y coordinate is determined by taking the middle y coordinate between y_{min} and y_{max} . On the other hand, the coordinate of v_2 is taken from the middle x coordinate of x_{min} and x_{max} and its y coordinate is determined by taking $\frac{7}{8}$ of the distance from y_{min} to y_{max} . Mathematically, these can be represented in equations (1), (2), (3) and (4).

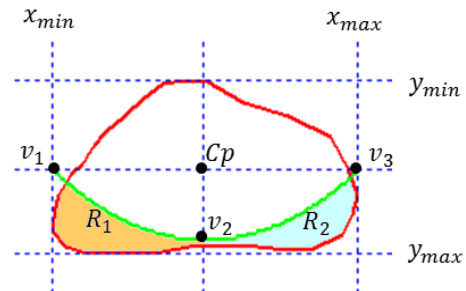


Figure 3: Prostate gland (red) and the defined PZ below $y = ax^2 + bx + c$ (green) which goes through v_1, v_2 and v_3 .

$$C_p = ((x_{min} + x_{max})/2, (y_{min} + y_{max})/2) \quad (1)$$

$$v_1 = (x_{min}, (y_{min} + y_{max})/2) \quad (2)$$

$$v_2 = ((x_{min} + x_{max})/2, y_{min} + ((y_{max} - y_{min}) \times \frac{7}{8})) \quad (3)$$

$$v_3 = (x_{max}, (y_{min} + y_{max})/2) \quad (4)$$

where C_p is the central point of the prostate. Once the coordinates of v_1, v_2 and v_3 are defined, we can

determine the values of a , b and c (therefore a final quadratic equation is defined). Finally, by taking every x coordinate from x_{min} to x_{max} into quadratic equation we are able to determine the y coordinate which will define the boundary of R_1 and R_2 . R_1 (amber region) and R_2 (turquoise region) are represented by left and right regions, respectively. By comparing the information obtained from R_1 and R_2 we estimate the presence of abnormalities.

3 PROPOSED METHODOLOGY

In summary, the proposed methodology starts by extracting two features from the original image followed by smoothing each of the extracted features. Subsequently, we performed peak detection within R_1 and R_2 for both features. Finally, based on the peak information obtained, a decision is made as to whether an abnormality is present.

3.1 Features

In many image analysis techniques, features representing specific image aspects are important in capturing information representing all textures. This process can be done using several techniques such as Gabor Filters (Zheng et al., 2004) (Jain and Karu, 1996), Grey Level Co-occurrence Matrix (GLCM) (Haralick et al., 1973) (Soh and Tsatsoulis, 1999) (Clausi, 2002) and Local Binary Pattern (LBP) (Lahdenoja et al., 2005). According to (Edge et al., 2010) and (Halpern et al., 2002) most prostate cancers in the PZ tend to have a dark appearance and several studies suggested that prostate cancer tissues tend to appear darker on a T2-weighted MRI image (Garnick et al., 2012) (Ginat et al., 2009) (Bast et al., 2000). In fact, radiologists also tend to use darker regions to identify abnormality within the PZ (Taneja, 2004). In another study (Vos et al., 2010) showed a potential method to detect prostate cancer by using blob and peak detectors on dark blob-like regions within apparent diffusion coefficient (ADC) map. This section presents our features which are based on low intensities to capture cancerous tissues followed by peak detection which will be explained in the next section.

In the proposed method, before features are extracted we performed noise reduction using median filtering. Median filtering takes the median intensity value of the pixels within the window as an output intensity of the pixel being processed. We used median filtering as it can smooth pixels whose values differ significantly from their surroundings without affecting the other pixels (Ekstrom, 1984). Subsequently,

we extracted two features which are f_{low} and f_{dif} . Firstly, f_{low} is calculated based on a sum of two vectors (McAllister and Bellittiere, 1996) which can be computed using

$$f_{low}(p, q) = \frac{1}{N} \sum_{b=1}^N \sqrt{(i_c)^2 + (i_b)^2} \quad (5)$$

where i_b is the intensity values of the b^{th} neighbour, i_c is the intensity value of the central pixel and $f_{low}(p, q)$ represents a new intensity value at position (p, q) . In addition, N is the number of neighbours which have intensity values less than the intensity value of the central pixel. This means, f_{low} represents the average of the sum vector of the central pixel with each of its neighbours which have lower intensity value than the central pixel. f_{low} contains most of the low intensities (higher probability of cancer). In order to extract the feature we run a small 5×5 sliding window over the original image (I). Figure 4 shows an example of how $f_{low}(p, q)$ is calculated for a 3×3 window.

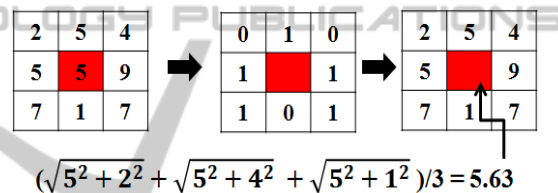


Figure 4: $f_{low}(p, q)$ is calculated using equation (5) by taking only those neighbours which have a value smaller than the central pixel.

On the other hand, the second feature (f_{dif}) is calculated by subtracting f_{min} from each of the elements in f_{low} . This means, f_{dif} contains the information difference between the sum vector and the minimum value. f_{min} can be calculated by taking the minimum value within a window.

$$f_{min}(p, q) = \min \{g(k, l)\} \quad (6)$$

where g is a window, $g(k, l) \in I$, I is the original image and k and l is the dimension of the window used. Once f_{min} is extracted we calculate f_{dif} using the following equation

$$f_{dif}(p, q) = f_{low}(p, q) - f_{min}(p, q) \quad (7)$$

This means, f_{dif} contains the difference between f_{low} and f_{min} . f_{dif} represents lower intensities than the ones in f_{low} (this will enhance our chance to capture more cancerous tissues). For example, based on Figure 4 $f_{min}(p, q) = 1$ and $f_{low}(p, q) = 5.63$, therefore $f_{dif}(p, q) = 4.63$. Since we have two features (f_{low} and f_{dif}) for each region R_1 and R_2 , from now on we use R_1^f and R_2^f to represent R_1 and R_2 for each feature, where $r \in \{low, dif\}$. Figure 5 shows examples

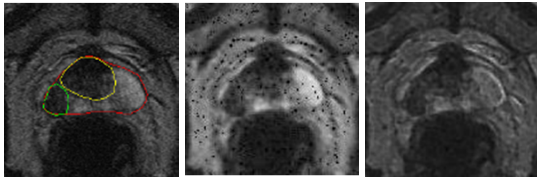


Figure 5: From left is original image, f_{low} and f_{dif} , respectively.

of features extracted from I . Note that, many black spots appeared in f_{low} . This is due to the effect in (5) (e.g. if i_c is smaller than all of its neighbours values). Since this will affect the peak detection results, smoothing/noise reduction is necessary to reduce this problem.

3.2 Feature Smoothing

According to (Hardle, 1991), feature smoothing is a process to minimise noise in an image while keeping the most important aspects of a dataset. In the proposed algorithm, we used two-stage noise reduction (Rampun et al., 2013b) based on a discrete cosine transform (DCT) followed by replacement of each pixel by the average of the neighbouring pixel values (using a 5×5 window). The complete explanation of DCT can be found in (Cabeen and Gent, 2012). Despite its good performance, DCT does not specify Q (the amount of smoothing/compression) automatically (Watson, 1993), which mainly affects the final result of the smoothed image. Garcia's modified method (Garcia, 2010) (based on DCT) uses a smoothing parameter that minimises the generalized cross-validation (GCV) score to estimate the amount of smoothing carried out in order to avoid over- or under-smoothing. Finally, Garcia's method is robust in dealing with weighted, missing, and outlier values by using an iterative procedure (Garcia, 2010). Figure 6 shows an example of f_{low} after smoothed.

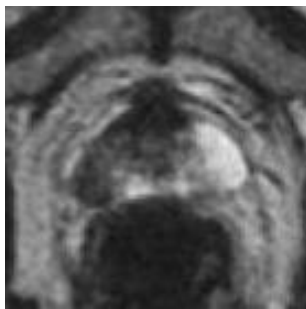


Figure 6: Smoothed f_{low} using DCT. Note that the small black spots/region (Figure 5) have disappeared.

3.3 Peak Detection

Peak detection is the process of finding local maxima and minima of a signal that satisfy certain properties (Instruments, 2013). Even though peak detection is less popular in medical image analysis, there are numerous methods have been developed particularly in signal processing (Latha et al., 2011). In signal processing, peak detection is widely used to capture signal fluctuation by measuring its properties such as positions, heights and widths. A common way to perform this technique is to make use of the fact that the first derivative of a peak has a downward-going zero-crossing at the peak maximum. Figure 7 shows an example of f_{low} within R_1 before and after smoothing. In the proposed method we applied peak detection in-

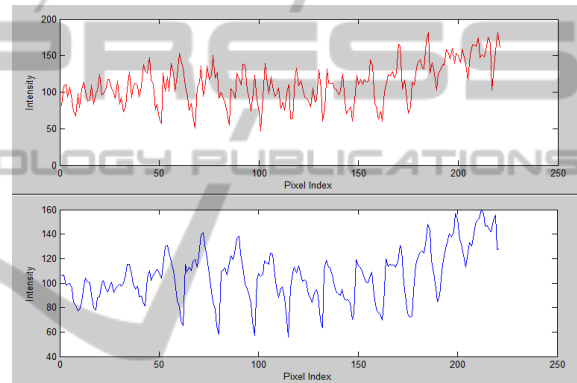


Figure 7: Unsmooth and smoothed signal represents in red and blue line, respectively. Fewer peaks are detected within the smoothed signal (blue) which is basically reduce the number of false zero-crossing.

dividually within R_1 and R_2 for each of the features. Since we are using Ochiai coefficient (Ochiai, 1957) to measure the similarity between two sets of vectors, we need to vectorise R_1 and R_2 ($\vec{R}_1^{f_r}$ and $\vec{R}_2^{f_r}$, respectively) by taking each element from top to bottom, left to right. Each element in $\vec{R}_1^{f_r}$ will be compared to its neighboring values. If an element is larger than both of its neighbors, the element is a local peak (MathWorks, 2013). Mathematically, a peak is defined as $\vec{R}_1^{f_r}(p, q) > \vec{R}_1^{f_r}(p, q+1)$ and $\vec{R}_1^{f_r}(p, q) > \vec{R}_1^{f_r}(p, q-1)$. This is the same for in $\vec{R}_2^{f_r}(p, q)$.

3.4 Abnormality Detection

In the proposed method, abnormality detection is performed by comparing the peak information obtained from $\vec{R}_1^{f_r}$ and $\vec{R}_2^{f_r}$. We calculated the following information

1. The Ochiai coefficient (O^{f_r}) (Ochiai, 1957) between $\vec{R}_1^{f_r}$ and $\vec{R}_2^{f_r}$ which is similar to the cosine

similarity (Zhu et al., 2010). The Ochiai coefficient measures the similarity between two sets of vectors. In principle, any type of similarity coefficient can be used, however we chose Ochiai coefficient because several experiments (Abreu et al., 2006) (Abreu et al., 2009) have shown that its performance is better than some other coefficient (Hofer and Wotawa, 2012) such as Tarantula (Jones and Harrold, 2005) and Jaccard (Yue and Clayton, 2005). The Ochiai coefficient indicates, the higher the value the more similar the elements in \vec{R}_1^{fr} and \vec{R}_2^{fr} which lead to a lower possibility of the prostate being abnormal.

2. The percentage (S) of elements in \vec{R}_2^{dif} that fall within the range of elements in \vec{R}_1^{dif} (if $\vec{R}_2^{dif} > \vec{R}_1^{dif}$). The higher the percentage the lower the difference between \vec{R}_1^{dif} and \vec{R}_2^{dif} which means a lower possibility of the prostate being abnormal.

We will explain how each of the above metrics is calculated in this section. The Ochiai coefficient is defined as

$$O = \frac{\#(A \cap B)}{\sqrt{\#(A) \times \#(B)}} \quad (8)$$

where A and B are sets which are represented as vectors and $\#(A)$ and $\#(B)$ are the number of elements in A and B , respectively. However, since the values in \vec{R}_1^{fr} and \vec{R}_2^{fr} are real values (e.g. 3.123) it is impossible to calculate $\#(A \cap B)$. On the other hand, we only take elements in \vec{R}_n^{fr} which are within the $minLimit$ and $maxLimit$ of each vector. This means, peaks with values outside the range will be ignored to ensure that we are considering only reliable peaks and minimise the effect of noise. We summarise each step for \vec{R}_n^{flow} ,

1. Find the range of \vec{R}_1^{flow} and \vec{R}_2^{flow} .

$$range_n = \max\{\vec{R}_n^{flow}\} - \min\{\vec{R}_n^{flow}\} \quad (9)$$

where max and min are the maximum and minimum values in \vec{R}_n^{flow} . Assuming that, \vec{R}_2^{flow} has the smaller range value.

2. Since \vec{R}_2^{flow} has a smaller range, find its $minLimit$ and $maxLimit$ values (if \vec{R}_1^{flow} has smaller range, find its $minLimit$ and $maxLimit$ values instead).

$$minLimit_{\vec{R}_2^{flow}} = \mu_{\vec{R}_2^{flow}} - \sigma_{\vec{R}_2^{flow}} \quad (10)$$

$$maxLimit_{\vec{R}_2^{flow}} = \mu_{\vec{R}_2^{flow}} + \sigma_{\vec{R}_2^{flow}} \quad (11)$$

$$\mu_{\vec{R}_2^{flow}} = \frac{1}{N} \sum \vec{R}_2^{flow}(p, q) \quad (12)$$

$$\sigma_{\vec{R}_2^{flow}} = \sqrt{\frac{1}{N} \sum (\vec{R}_2^{flow}(p, q) - \mu_{\vec{R}_2^{flow}})^2} \quad (13)$$

where μ and σ represent the mean and standard deviation of \vec{R}_2^{flow} .

3. Calculate the Ochiai coefficient using

$$O^{flow} = \frac{\#(\vec{R}_1^{flow} \leq \vec{R}_2^{flow} \leq \vec{R}_1^{flow})}{\sqrt{(\#(\vec{R}_1^{flow}) \times \#(\vec{R}_2^{flow}))}} \quad (14)$$

where $\#(\vec{R}_1^{fr} \geq \vec{R}_2^{fr} \leq \vec{R}_1^{fr})$ represents the number of elements in \vec{R}_1^{fr} which is within $minLimit_{\vec{R}_2^{fr}}$ and $maxLimit_{\vec{R}_2^{fr}}$.

The steps are the same for the second feature (f_{dif}) in \vec{R}_n^{dif} . Next, we calculate S (the maximum value is 100) using

$$S = \frac{\#(\vec{R}_1^{fr} \geq \vec{R}_2^{fr} \leq \vec{R}_1^{fr})}{H} \times 100 \quad (15)$$

where

$$H = \begin{cases} \#\vec{R}_1^{dif}, & \text{if } \#\vec{R}_1^{dif} > \#\vec{R}_2^{dif} \\ \#\vec{R}_2^{dif}, & \text{otherwise} \end{cases} \quad (16)$$

The decision whether abnormality is present or not is based on the flow chart in Figure 8.

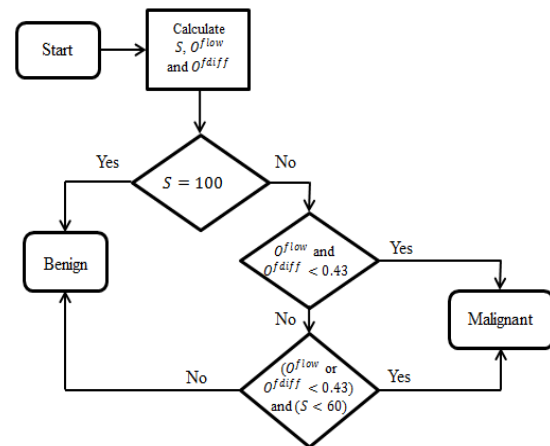


Figure 8: Flow chart decision rule.

Based on the conditions above, it shows that a slice is malignant if both O^{flow} and O^{dif} are smaller than the threshold value (we selected this parameter value as 0.43 as this produced the highest correct classification rate based on 101 different thresholds tested (see Figure 14)) or if O^{flow} or O^{dif} are below the threshold value and S below 60 (we chose this parameter value as it produced the highest accuracy of $\approx 70\%$ based on 10 different thresholds (10 to 100)

tested. The experiment was performed by classifying every single case using a single S value and selecting the one with the highest classification rate. This experiment is exactly the same when selecting the value of O^{flow} and O^{dif} . This means, if any of O^{flow} or O^{dif} value is smaller than the threshold, we will use S to determine the occurrence of abnormalities. Nevertheless, if $S = 100$, we do not have a need to check O^{fr} because it indicates the maximum similarity percentage. Finally, if the third condition in Figure 8 is passed then the slice is considered benign.

4 EXPERIMENTAL RESULTS

This section presents our experimental results. In total, our database contains 90 prostate T2-Weighted MRI images (512×512) from 25 different patients aged 54 to 74. Each patient has 3 to 5 slices through the central part of the prostate. The prostates, cancer and central zones were delineated by an expert radiologist on each of the MRI images. Data was analysed and classified as to whether the prostate contains cancer based on the conditions explained previously. Subsequently, we compared the result with the ground truth whether the prostate contains cancer regions or not. We will present two different cases and the justification for the threshold values selection. The first case (Figure 9) shows the results of a slice with cancer. Figure 9 shows the original image

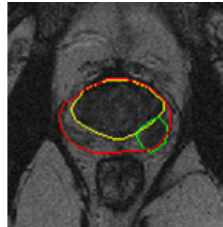


Figure 9: Case # 1: Malignant.

(top) with ground truth, prostate gland (red), CZ (yellow) and tumor (green). Figure 10 shows results of \vec{R}_n^{flow} and \vec{R}_n^{dif} , respectively. Black and magenta represent \vec{R}_1^{fr} and \vec{R}_2^{fr} . On the other hand, $maxLimit_{\vec{R}_n^{fr}}$ and $minLimit_{\vec{R}_n^{fr}}$ are represented in the lines which are parallel with the x axis (broken lines). Note that we use the same order and notations for the second case as well. From Figure 10 we can visually identify that most values in \vec{R}_1^{fr} and \vec{R}_2^{fr} are quite separated in both features. By calculating the metrics defined in section 3.4, we will get the following results: $O^{flow} = 0.177$, $O^{dif} = 0.367$ and $S = 35.71\%$. Therefore the slice is considered malignant based on the conditions shown

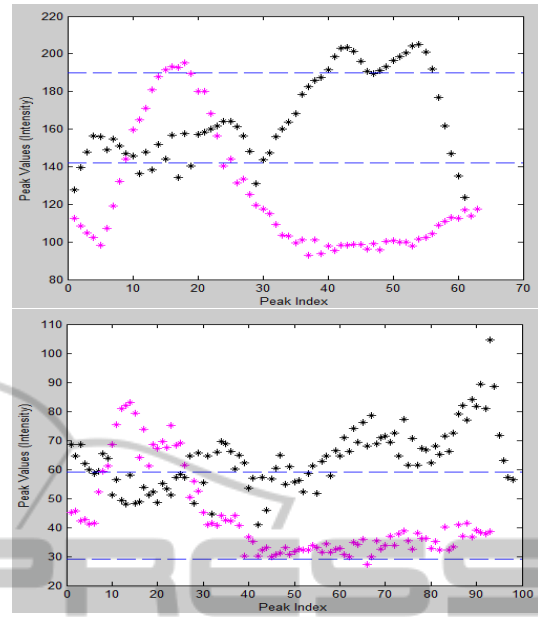


Figure 10: Results of case # 1: Malignant.

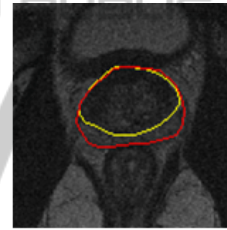


Figure 11: Case # 2: Benign.

in section 3.4.

On the other hand, Figures 11 and 12 show an example of a slice without an abnormality and its results, respectively. In this example, we can see that $\approx 95\%$ of the values in \vec{R}_1^{fr} and \vec{R}_2^{fr} are within the same range (Figure 12). By calculating the metrics we will get the following results: $O^{flow} = 0.77$, $O^{dif} = 0.81$ and $S = 72.44\%$. Therefore, the slice is considered benign because all metric values are above the threshold values.

Figure 13 shows the Receiver Operating Characteristic (ROC) curves of the proposed method based on 101 different threshold values. The minimum and maximum threshold values are 0 and 1, respectively with 0.01 difference between threshold values. The ROC graph shows that the proposed method achieved 0.80 true positive rate with 0.20 false positive rate. In terms of correct classification rate (CCR) against different thresholds, Figure 14 shows that $O^{fr} < 0.43$ achieved the highest CCR of 82.2%. On the other hand, Figure 14 shows the boxplot of O^{flow} and O^{dif} for benign (blue) and malignant (red) cases. Based on the results in Figure 14, it is clearly shows that most

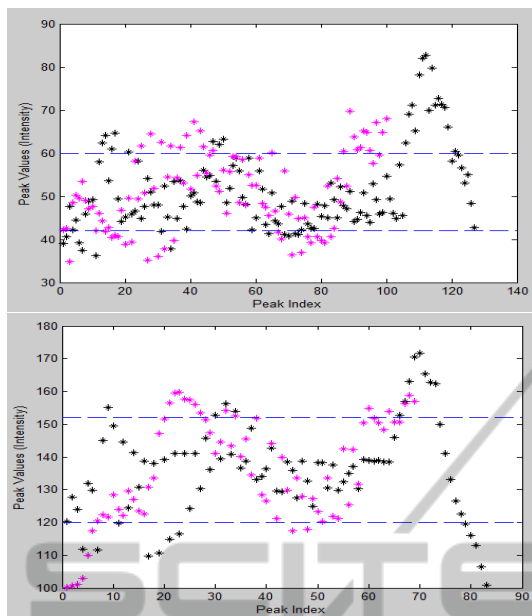


Figure 12: Results of case # 2: Benign.

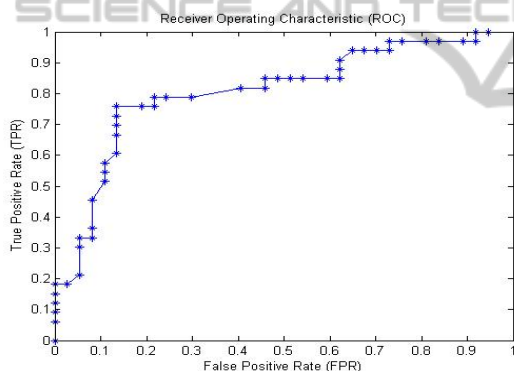


Figure 13: ROC curves of the proposed method using 101 different threshold values (O^{fr}).

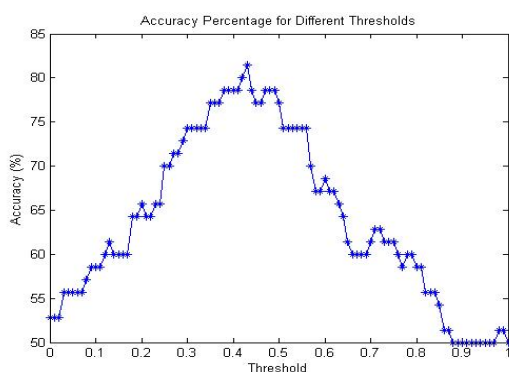


Figure 14: Accuracies of the proposed method using 101 different threshold values (O^{fr}).

benign cases have $O^{fr} > 0.4$ between \vec{R}_1^{fr} and \vec{R}_2^{fr} . Similarly the results in Figure 15 shows that most be-

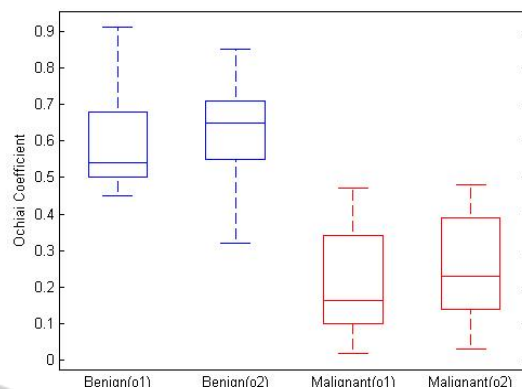


Figure 15: O^{flow} and O^{dif} represented in o1 and o2, respectively.

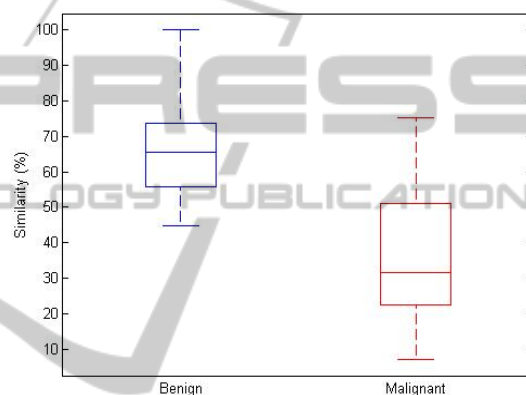


Figure 16: Similarity percentage (S) (between \vec{R}_1^{fr} and \vec{R}_2^{fr}) for benign and malignant cases represented in blue and red, respectively.

nign cases have $S > 60$ compared to malignant cases which have $S < 60$.

For the 90 prostate MRI slices from 25 different patients (41 slices are malignant and 49 slices are benign), the proposed method achieved 82.2% (74 slices classified correctly). On the other hand, the proposed method produced 8.9% false negative and false positive results. Since, the number of methods which uses peak detection methods (in medical image analysis applications) in the literature is limited, it is hard to make a direct comparison with other methods. In addition, different datasets and frameworks used in the literature also make it extremely difficult to perform a qualitative comparison. However, to compare our results indirectly with some existing methods we cite several methods which have a similar goal (detecting prostate abnormality/cancer).

Table 1 presents the experimental results of ten different methods (included our method) and their average accuracies. Note that every method used different datasets, modalities and frameworks. The

Table 1: First, second and third column represents the authors, number of prostates and average accuracy (AA), respectively.

Authors	# of cases	AA (%)
(Sung et al., 2011)	42	89
(Vos et al., 2010)	29	89
(Reinsberg et al., 2007)	42	87
(Rampun et al., 2013a)	19	85
(Ampeliotis et al., 2007)	10	84
Our method	25	82
(Castaneda et al., 2009)	15	80
(Litjens et al., 2011)	188	79
(Tiwari et al., 2007)	14	78
(Llobet et al., 2007)	303	62

methods proposed by (Sung et al., 2011) and (Vos et al., 2010) achieved the highest average accuracy of 89% whereas the methods by (Llobet et al., 2007), (Tiwari et al., 2007), (Litjens et al., 2011) failed to achieve more than 80% accuracy. On the other hand, the proposed method achieved 0.81 sensitivity and 0.84 specificity which is similar with the recent method proposed by (Artan and Yefik, 2012). (Girouin et al., 2007) reports sensitivity/specificity value of 0.5-0.6 and 0.13-0.21 over 46 patients using only T2-weighted (1.5 T) MRI. Further, (Girouin et al., 2007) presents a higher both sensitivity and specificity 0.83 for the same number of patients using T2-weighted (3.0 T) MRI. In a smaller dataset (Fitterer et al., 2006) presents 0.83 both on sensitivity and specificity, respectively. In a different modality, (Wong and Scharcanski, 2011) shows a higher sensitivity (0.93) and specificity (0.96) in 46 ultrasound images. As mentioned earlier, these comparisons are very subjective as accuracy, sensitivity and specificity are highly influenced by the number of datasets, different modalities and methods' frameworks. Therefore it is extremely difficult to make a real comparison either quantitatively or qualitatively. Some obvious drawbacks of the proposed method, it failed to produce accurate results in two cases: a) when the prostate's peripheral zone is almost non-existent, and b) when the prostate's shape does not conform to the shape of our prostate model.

5 CONCLUSIONS

The proposed method shows that peak information has a potential role in detecting prostate abnormalities within the PZ. In contrast with some of the methods in Table 1, our method uses a minimal set of features and modalities (only T2-Weighted MRI). Methods by

(Engelbrecht et al., 2010) and (Vos et al., 2010) used multimodalities data such as diffusion MRI, MR spectroscopy and a combination of T1 and T2-weighted imaging. Secondly, the proposed method does not use any supervised/unsupervised classifiers for classification but it is entirely dependent on the metric values computed from the peak information. Moreover, our method does not refer to or use any clinical features in making decision as to whether abnormality occurs but is entirely based on the values of O^{fr} and S . The method of (Vos et al., 2010) used clinical features such as PSA level to support their method in making decision whether abnormality is truly present or not. Nevertheless, one obvious drawback of our method is that it does not have an additional method to reduce false positive and false negative results. Therefore a robust false positive/negative reduction method is needed to increase the accuracy rate. Secondly, if the tumor appears outside the R_1 and R_2 regions the method failed to identify the abnormality due to the incorrect information captured. To solve this issue, we are developing a segmentation method to separate CZ from prostate gland. This allows the proposed method to be more robust because it will analyse regions within the prostate (therefore improving the 2D PZ model will be apart of our future work).

In short, with 8.9% false negative and false positive results (sensitivity/specificity: 0.81/0.84), the proposed method achieved similar accuracy with some of the methods in the literature. In our study, we have shown that most MRI slices containing cancer have small value of Ochiai coefficient ($O^{fr} < 0.43$) and $S < 60\%$. This means, if the coefficient between \vec{R}_1^{fr} and \vec{R}_2^{fr} is less than a threshold value (in our case 0.43), the prostate has a higher probability to be abnormal. Moreover, a similarity percentage less than 60% also indicate prostate abnormality. Finally, the next stage of this research is to test the proposed method on a larger dataset with a combination of several methods (e.g. CZ segmentation, false positive/negative reduction, and blob detection), improving the 2D PZ model and other statistical features (e.g. entropy and energy).

REFERENCES

- Abreu, R., Zoetewij, P., Golsteijn, R., and van Gemund, A. J. (2009). A practical evaluation of spectrum-based fault localization. *Journal of Systems and Software*, 82(11):1780 – 1792. `je:ce:title;SI: {TAIC} {PART} 2007 and {MUTATION} 2007;ce:title;`
- Abreu, R., Zoetewij, P., and Van Gemund, A. J. C. (2006). An evaluation of similarity coefficients for software fault localization. In *Dependable Computing, 2006*.

- PRDC '06. 12th Pacific Rim International Symposium on*, pages 39–46.
- Ampeletis, D., Antonakoudi, A., Berberidis, K., and Psarakis, E. Z. (2007). Computer aided detection of prostate cancer using fused information from dynamic contrast enhanced and morphological magnetic resonance images. In *IEEE International Conference on Signal Processing and Communications (ICSPC 2007)*.
- Artan, Y. and Yetik, I. (2012). Prostate cancer localization using multiparametric mri based on semisupervised techniques with automated seed initialization. *Information Technology in Biomedicine, IEEE Transactions on*, 16(6):1313–1323.
- Aus, G., Hermansson, C. G., Hugosson, J., and Pedersen, K. V. (2008). Transrectal ultrasound examination of the prostate: complications and acceptance by patients. *British journal of urology*, 71(4):457–459.
- Bast, R. C., Kufe, D. W., Pollock, R. E., Weichselbaum, R. R., Holland, J. F., Frei, E., Halvorsen, R. A., and Thompson, W. M. (2000). Imaging neoplasms of the abdomen and pelvis.
- Brawer, M. K. (1991). Prostate specific antigen: A review. *Acta Oncologica*, 30(2):161–168.
- Cabeen, K. and Gent, P. (2012). Image compression and the Discrete Cosine Transform. <http://www.lokminglui.com/dct.pdf/>. Accessed 11-August-2013.
- Castaneda, B., An, L., Wu, S., Baxter, L. L., Yao, J. L., Joseph, J. V., Hoyt, K., Strang, J., Rubens, D., and Parker, K. J. (2009). Prostate cancer detection using crawling wave sonoelastography. In *Proc. SPIE 7265, Medical Imaging 2009: Ultrasonic Imaging and Signal Processing*.
- Choi, Y. F., Kim, F. K., Kim, N., Kim, K. W., Choi, E. K., and Cho, K.-S. (2007). Functional MR imaging of prostate cancer. *RadioGraphics*, 27(1):63–68.
- Clausi, D. A. (2002). An analysis of co-occurrence texture statistics as a function of grey level quantization. *Can. J. Remote Sensing*, 28(1):45–62.
- Edge, S. B., Byrd, D. R., Compton, C., Fritz, A. G., Greene, F. L., and Trotti, A. (2010). *AJCC Cancer Staging Manual (7th Edition)*. Springer., Chicago, US.
- Ekstrom, P. M. (1984). *Digital Image Processing Techniques*. Academic Press, Inc., London, UK.
- Engelbrecht, M. R., Puech, P., Colin, P., Akin, O. Lemaitre, L., and Villers, A. (2010). Multimodality magnetic resonance imaging of prostate cancer. *Journal of endourology society*, 24(5):677–684.
- Ftterer, J. J., Heijmink, S. W. T. P. J., Scheenen, T. W. J., Veltman, J., Huisman, H. J., Vos, P., de Kaa, C. A. H., Witjes, J. A., Krabbe, P. F. M., Heerschap, A., and Barentsz, J. O. (2006). Prostate cancer localization with dynamic contrast-enhanced mr imaging and proton mr spectroscopic imaging. *Radiology*, 241(2):449–458. PMID: 16966484.
- Garcia, D. (2010). Robust smoothing of gridded data in one and higher dimensions with missing values. *Computational Statistics and Data Analysis*, 54(4):1167–1178.
- Garnick, M. B., MacDonald, A., Glass, R., and Leighton, S. (2012). *Harvard Medical School 2012 Annual Report on Prostate Diseases*. Harvard Medical School, Harvard, US.
- Ginat, D. T., Destounis, S. V., Barr, R. G., Castaneda, B., Strang, J. G., and Rubens, D. J. (2009). Us elastography of breast and prostate lesions. *Radiographics*, 29(7):2007–2016.
- Girouin, N., Mège-Lechevallier, F., Senes, A. T., Bissery, A., Rabilloud, M., Maréchal, J., Colombel, M., Lyonnet, D., and Rouvière, O. (2007). Prostate dynamic contrast-enhanced mri with simple visual diagnostic criteria: is it reasonable? *European radiology*, 17(6):1498–1509.
- Halpern, E. J., Cochlin, D. L., and Goldberg, B. (2002). *Imaging of the Prostate*. Martin Dunitz Ltd., London, UK.
- Haralick, R. M., Shanmugam, K., and Dinstein, I. (1973). Textural features for image classification. *IEEE Transactions On Systems, Man, and Cybernetics*, 3(6):610–621.
- Hardle, W. (1991). *Smoothing Techniques With Implementation in S*. Springer-Verlag., Louvain-La-Neuve, Belgium.
- Hofer, B. and Wotawa, F. (2012). Spectrum enhanced dynamic slicing for better fault localization. In *ECAI*, pages 420–425.
- Instruments (2013). Wavelet-based peak detection. <http://www.ni.com/white-paper/5432/en/>. Accessed 24-July-2013.
- Jain, A. K. and Karu, K. (1996). Learning texture discrimination. *IEEE Transactions on Pattern Analysis and Machine Intelligence*, 18:195–205.
- Jones, J. A. and Harrold, M. J. (2005). Empirical evaluation of the tarantula automatic fault-localization technique. In *Proceedings of the 20th IEEE/ACM International Conference on Automated Software Engineering, ASE '05*, pages 273–282, New York, NY, USA. ACM.
- Kenny, T. (2012). Prostate cancer. <http://www.patient.co.uk/health/prostate-cancer/>. Accessed 12-August-2013.
- Lahdenoja, O., Laiho, M., and Paasio, A. (2005). Local binary pattern feature vector extraction with cnn. In *9th International Workshop on Cellular Neural Networks and Their Applications*, pages 202–205. IEEE Cat.
- Latha, I., Reichenbach, S. E., and Tao, Q. (2011). Comparative analysis of peak-detection techniques for comprehensive two-dimensional chromatography. *RadioGraphics*, 1218(38):6792–6798.
- Litjens, G. J. S., Vos, P. C., Barentsz, J. O., Karssemeijer, N., and Huisman, H. J. (2011). Automatic computer aided detection of abnormalities in Multi-Parametric prostate MRI. In *Proc. SPIE 7963, Medical Imaging 2011: Computer-Aided Diagnosis*.
- Llobet, R., Juan, C., Cortes, P., Juan, A., and Toselli, A. (2007). Computer-aided detection of prostate cancer. *International Journal of Medical Informatics*, 76(7):547–556.
- MathWorks (2013). Documentation center: findpeaks.

- <http://www.mathworks.co.uk/help/signal/ref/findpeaks.html/>. Accessed 23-August-2013.
- McAllister, H. C. and Bellittiere, D. (1996). The sum of two vectors. <http://www.hawaii.edu/suremath/jsumTwoVectors.html>. Accessed 19-August-2013.
- Ochiai, A. (1957). Zoo geographical studies on the solenoid fishes found Japan and its neighboring regions.ii. *Bull.Japan.Soc.Sci.Fisheries.*, 22(9):526–530.
- PCUK (2013). Prostate cancer facts and figures. <http://prostatecanceruk.org/information/prostate-cancer-facts-and-figures/>. Accessed 11-August-2013.
- Rampun, A., Chen, Z., and Zwiiggelaar, R. (2013a). Detection and localisation of prostate abnormalities. In *3rd International Conference on Computational & Mathematical Biomedical Engineering, CMBE 13*.
- Rampun, A., Strange, H., and Zwiiggelaar, R. (2013b). Texture segmentation using different orientations of GLCM features. In *6th International Conference on Computer Vision / Computer Graphics Collaboration Techniques and Applications, MIRAGE 13*.
- Reinsberg, S. A., Payne, G. S., Riches, S. F., Ashley, S., Brewster, J. M., Morgan, V. A., and deSouza, N. M. (2007). Combined use of Diffusion-Weighted MRI and 1H MR Spectroscopy to increase accuracy in prostate cancer detection. *American Journal of Roentgenology*, 188(1):1122–1129.
- Roehl, K. A., Antenor, J. A. V., and Catalona, W. J. (2002). Serial biopsy results in prostate cancer screening study. *British journal of urology*, 167(6):2435–2439.
- Shirley, A. and Brewster, S. (2011). Expert review: The digital rectal examination. *Journal of Clinical Examination*, 11:1–12.
- Soh, L. and Tsatsoulis, C. (1999). Texture analysis of sar sea ice imagery using gray level co-occurrence matrices. *Geoscience and Remote Sensing, IEEE Transactions on*, 37(2):780–795.
- Sung, Y. S., Kwon, H.-J., Park, B. W., Cho, G., Lee, C. K., Cho, K.-S., and Kim, J. K. (2011). Prostate cancer detection on dynamic contrast-enhanced mri: Computer-aided diagnosis versus single perfusion parameter maps. *American Journal of Roentgenology*, 197(5):1122–1129.
- Taneja, S. S. (2004). Imaging in the diagnosis and management of prostate cancer. *Reviews in Urology*, 6(3):101.
- Tempany, C. and Franco, F. (2012). Prostate MRI: Update and current roles. *Applied Radiology*, 41(3):17–22.
- Tidy, C. (2013). Prostate specific antigen (PSA) test. <http://www.patient.co.uk/health/prostate-specific-antigen-psa-test/>. Accessed 12-August-2013.
- Tiwari, P., Madabhushi, A., and Rosen, M. (2007). A hierarchical unsupervised spectral clustering scheme for detection of prostate cancer from magnetic resonance spectroscopy (MRS). In *Medical Image Computing and Computer Assisted Intervention (MICCAI)*, pages 278–286.
- Vos, P. C., Hambrock, T., Barentsz, J., and Huisman, H. (2010). Computer-assisted analysis of peripheral zone prostate lesions using T2-weighted and dynamic contrast enhanced T1-weighted MRI. *Physics in Medicine and Biology*, 55:1719–1734.
- Watson, A. B. (1993). Dctune: A technique for visual optimization of dct quantization matrices for individual images. *Society for Information Display Digest of Technical Papers*, XXIV:946–949.
- Wong, A. and Scharcanski, J. (2011). Fisher #x2013;tippett region-merging approach to transrectal ultrasound prostate lesion segmentation. *Information Technology in Biomedicine, IEEE Transactions on*, 15(6):900–907.
- Yue, J. C. and Clayton, M. K. (2005). A similarity measure based on species proportions. *Communications in Statistics - Theory and Methods*, 34(11):2123–2131.
- Zheng, D., Zhao, Y., and Wang, J. (2004). Feature extraction using a gabor filter family. In *Proceedings of the 6th IASTED International Conference on Signal and Image Processing*. The International Association of Science and Technology for Development.
- Zhu, S., Wu, J., and Xia, G. (2010). Top-k cosine similarity interesting pairs search. In *Seventh International Conference on Fuzzy Systems and Knowledge Discovery (FSKD)*.